A landslide dating framework using a combination of Sentinel-1 SAR and -2 optical imagery

Sheng Fu [a,*], Steven M. de Jong [a], Xuejiao Hou [b], Job de Vries [a], Axel Deijns [c,d], Tjalling de Haas [a]

[a] *Department of Physical Geography, Utrecht University, Princetonlaan 8a, 3584 CB Utrecht, Netherlands*
[b] *School of Geospatial Engineering and Science, Sun Yat-Sen University, 510275 Guangzhou, China*
[c] *Department of Earth Sciences, Royal Museum for Central Africa, 3080 Tervuren, Belgium*
[d] *Department of Hydrology and Hydraulic Engineering, Earth System Science, Vrije Universiteit Brussel, 6 1050 Elsene, Belgium*

ARTICLE INFO

ABSTRACT

Landslides are mass movements of rock or soil down a slope, which may cause economic loss, damage to natural resources and frequent fatalities. To support risk management, landslide dating methods can provide useful knowledge about the date of the landslide and the frequency of occurrences, and thus potential triggers. Remote sensing techniques provide opportunities for landslide dating and are especially valuable in remote areas. However, the use of optical remote sensing is frequently hampered by cloud cover, decreasing the success rate and accuracy of dating. Here, we propose a landslide dating framework that combines the advantages of optical and SAR remote sensing satellites, because optical monitoring provides spectral changes on the ground and microwave observations provide information on surface changes due to loss of coherence. Our method combines Sentinel-1 and -2 satellite data, and is designed for cases wherein the landslide causes vegetation decrease and terrain deformation resulting in changing Normalized Difference Vegetation Index (NDVI) and SAR backscatter values. This landslide dating framework was tested and evaluated against 60 published landslides across the world. We show that the mean accuracy of landslide dating reaches 23 days when using combined Sentinel-1 and -2 imagery, which is a pronounced improvement compared to using only optical Sentinel-2 images resulting in an accuracy of 51 days. This study highlights that a combination of optical and SAR remote sensing monitoring is a promising technique for dating landslides, especially in remote areas where monitoring equipment is limited or which are frequently covered by clouds. Our method contributes to identifying failure mechanism by providing reliable date ranges of landslide occurrence, assessing landslide hazard and constructing landslide early warning systems.

1. Introduction

Landslides, defined as mass movements of rock and soil down a slope (Fell et al., 2008; Varnes and the IAEG, 1984), are among the most common natural hazards around the world (Mondini et al., 2021). Because of their abrupt displacement, broad spatial extent and low predictability, landslides can result in loss of natural resources and property, and result in numerous casualties each year (CRED, 2018; Froude and Petley, 2018; Guo et al., 2020). The United Nations office for disaster risk reduction reported that landslides caused 18,414 deaths and affected 4.8 million people in the period of 1998–2017 (CRED, 2018), which is an underestimated number due to incomplete data availability. In addition, the Global Fatal Landslide Database shows that

around 56,000 people were killed by non-seismic landslides from 2004 to 2016 (Froude and Petley, 2018). In order to protect natural resources and residents, various landslide monitoring techniques have been developed to support the estimation of landslide hazard and risk (Angeli et al., 2000; Geertsema et al., 2009; Guzzetti et al., 2012). Landslide inventories enable landslide risk managers to have a good understanding of where and when landslides happened in the past (Guzzetti et al., 2012; Schlögel et al., 2015), providing valuable information for effective land-use planning and mitigating landslide hazards. Landslide dating aims to identify the most probable date of historic landslide occurrence by the approaches of field measurements, global navigation satellite systems, terrestrial laser scanning, airborne laser scanning, photogrammetry or by analysis of remote sensing satellite imagery (Akçar

---

et al., 2012; Pánek, 2015; Šilhán, 2020). Such dating information is crucial for landslide hazard assessment and might contribute to damage mitigation.

Remote sensing techniques can monitor landslide movement, in order to unravel the triggering conditions and mechanisms of landslides, to assess the evolution of landslides, and for landslide mapping in landslide-prone areas (Fell et al., 2008; van Westen et al., 2008; Xu et al., 2023). Compared to traditional field observations, remote sensing based monitoring is able to capture the complex characteristics of pre- and post-failure deformation and displacement efficiently in both spatial and temporal scales (Guo et al., 2020; Squarzoni et al., 2003; Tang et al., 2011; Xiong et al., 2020). As such, remote sensing is an important tool for landslide risk mitigation. Both optical and SAR remote sensing satellites enable periodic observations of the earth surface, making it possible to monitor natural hazards such as landslides (Zhao et al., 2023). Satellite image time series can record how slope characteristics evolve in space and time, and can thereby be used for landslide dating, and to track landslide deformation and displacement (Lu et al., 2021; Squarzoni et al., 2003).

There are three typical landslide dating approaches: (1) Dating geomorphic evidence, using radiocarbon dating (Ostermann et al., 2012), cosmic-ray exposure dating (Cossart et al., 2008), optically-stimulated luminescence dating (Akçar et al., 2012) and dendrochronology (Šilhán, 2020); (2) Ground-based monitoring to record landslide development (Angeli et al., 2000); (3) Remote sensing satellite imagery to monitor the reflectance signal from the ground surface. Compared to the former two dating approaches, remote sensing satellite monitoring approaches offer the unique opportunity to date landslide occurrences on a regional scale without having to visit the landslides and is especially valuable in remote and difficult to access areas. Satellite-based landslide dating techniques have previously been developed and implemented by using SAR (Synthetic Aperture Radar) (Burrows et al., 2022) or optical (Behling et al., 2016; Yang et al., 2019) sensors of remote sensing. However, the potential of combined approaches using the advantages of both SAR and optical remote sensing need to be further investigated (Casagli et al., 2016).

Optical satellites have the advantage of identifying land use and land cover change, and use that information to detect landslides (Geertsema et al., 2009; Guzzetti et al., 2012; Lu et al., 2021). Optical remote sensing techniques have been utilized to observe and analyze the evolution of landslides with a variation of objectives and applications. For example, manual investigation of optical remote sensing images is often used to get a quick overview of landslide impact directly following occurrence (Casagli et al., 2016; Yang et al., 2019). Furthermore, satellite images have been analyzed for quantification of landslide volume displacement (Dille et al., 2021), landslide or change detection mapping (Amatya et al., 2021), digital surface model generation (Mondini et al., 2021), landslide dating (Behling et al., 2016; Guzzetti et al., 2012), and monitoring lake formation after landslide dam formation (Fan et al., 2021). Spectral indices derived from optical remote sensing images such as the Normalized Difference Vegetation Index (NDVI; Tucker, 1979) are sensitive to vegetation and its changes, and thus capable of detecting landslide activity in vegetation-covered areas. When landslides occur in vegetated areas they typically (partly) remove or damage the vegetation. This decrease in vegetation density can be captured by optical remote sensing satellites, enabling dating of landslide occurrence. For example, by employing the Landsat archive (1982-present), (semi-)automatic landslide dating methods have been developed and successfully applied to the Buckinghorse River area, British Columbia, Canada (Deijns et al., 2020). These studies showed that the NDVI is a suitable index to detect landslide disturbance in a spruce / pine covered forest zones. For example, the SWADE (Segmented WAvelet-DEnoising and stepwise linear fitting) method compares the landcover on a landslide and the undisturbed vegetation directly next to the landslide in time series of optical satellite images (Fu et al., 2023). They tested this method on the Landsat image archive, but the moderate spatial resolution (30 m) and revisit time (16 days or more) of Landsat imagery limits the dating accuracy and minimum detectable size of landslides. Therefore, the Copernicus Sentinel-2 mission (European Space Agency, Europe Union), a constellation of two satellites, can be an apt improvement or supplement (Wang et al., 2022) due to its higher spatial resolution of 10 m, shorter revisit time of 5 days and improved multispectral band settings. Although Sentinel-2 has been shown to be applicable to monitor landslides (Fan et al., 2021; Lu et al., 2021; Qu et al., 2021), landslide dating by Sentinel-2 imagery has not yet been studied thoroughly. Furthermore, optical remote sensing images frequently suffer from cloud contamination (Frantz et al., 2018; Zhu, 2017; Zhu et al., 2015), especially around the rainfall-induced events that often trigger landslides, which may hamper detailed landslide dating.

Landslides can also be detected by SAR remote sensing satellites by using backscatter coefficients of multitemporal imagery. The microwave signal transmitted from the SAR sensors strikes the ground surface, and then returns to the SAR antenna recording useful geomorphological information and observing ground surface displacement or deformation. Microwave signals penetrate clouds and reflect against the land surface, generating cloud free observations of the earth surface. Thus, SAR imaging satellites can monitor the land cover change during all weather conditions and during day and night (Mullissa et al., 2021). SAR techniques have been applied to study landslides (Mondini et al., 2021), for example by coherence analysis (Squarzoni et al., 2003), Digital Elevation Model (DEM) reconstruction (Dai et al., 2019), and landslide surface displacements (Samsonov et al., 2020). The Sentinel-1 satellite is equipped with an 5.405GHz C-band instrument and ~ 5.6 cm wavelength, has a weekly revisit time and a high spatial resolution of 20×22 m (Mullissa et al., 2021) and provides valuable SAR backscatter information for landslide dating. Furthermore, amplitude and phase information can be used to determine the land cover type and surface roughness in different ways, and temporal changes therein may be used to date landslides. Nevertheless, landslide dating studies using the Sentinel-1 satellite are scarce (Burrows et al., 2022; Deijns et al., 2022).

Landslides are often triggered during extreme weather conditions. As a result, there are often relatively long periods between the nearest available cloud-free pre- and post-event optical satellite image, resulting in a reduced dating accuracy (Deijns et al., 2020). The dating-range accuracy may notably be improved by combining optical and SAR imagery, but this has not been explored in detail so far. The objective of this study is to present a suitable landslide dating framework combining SAR and optical remote sensing images acquired by Sentinel-1 and -2. Using the previously published SWADE method (Fu et al., 2023) we first generate a coarse date range of each landslide using optical Sentinel-2 images. Next, we apply a change vector index to the amplitude of SAR Sentinel-1 in this coarse data range to obtain a refined landslide occurrence date range defined by the largest change in SAR backscatter. We tested and evaluated our proposed landslide dating framework using 60 published landslides worldwide.

2. Methodology

To obtain the date range of landslide occurrence, ground surface disturbance evidence can be derived from the satellite imagery. This evidence details the landslide phenomenon of damaging vegetation partly (or entirely) and of causing topographic surface changes. According to these two types of evidence, the landslide dating framework is separated into two parts: analyses of optical imagery (section 2.1) followed by analyses of SAR imagery (section 2.2; Fig. 1). All the satellite imagery is amassed from Google Earth Engine (GEE), outputting the time series of NDVI and SAR amplitude for all 60 landslides in the validation dataset (section 2.3).
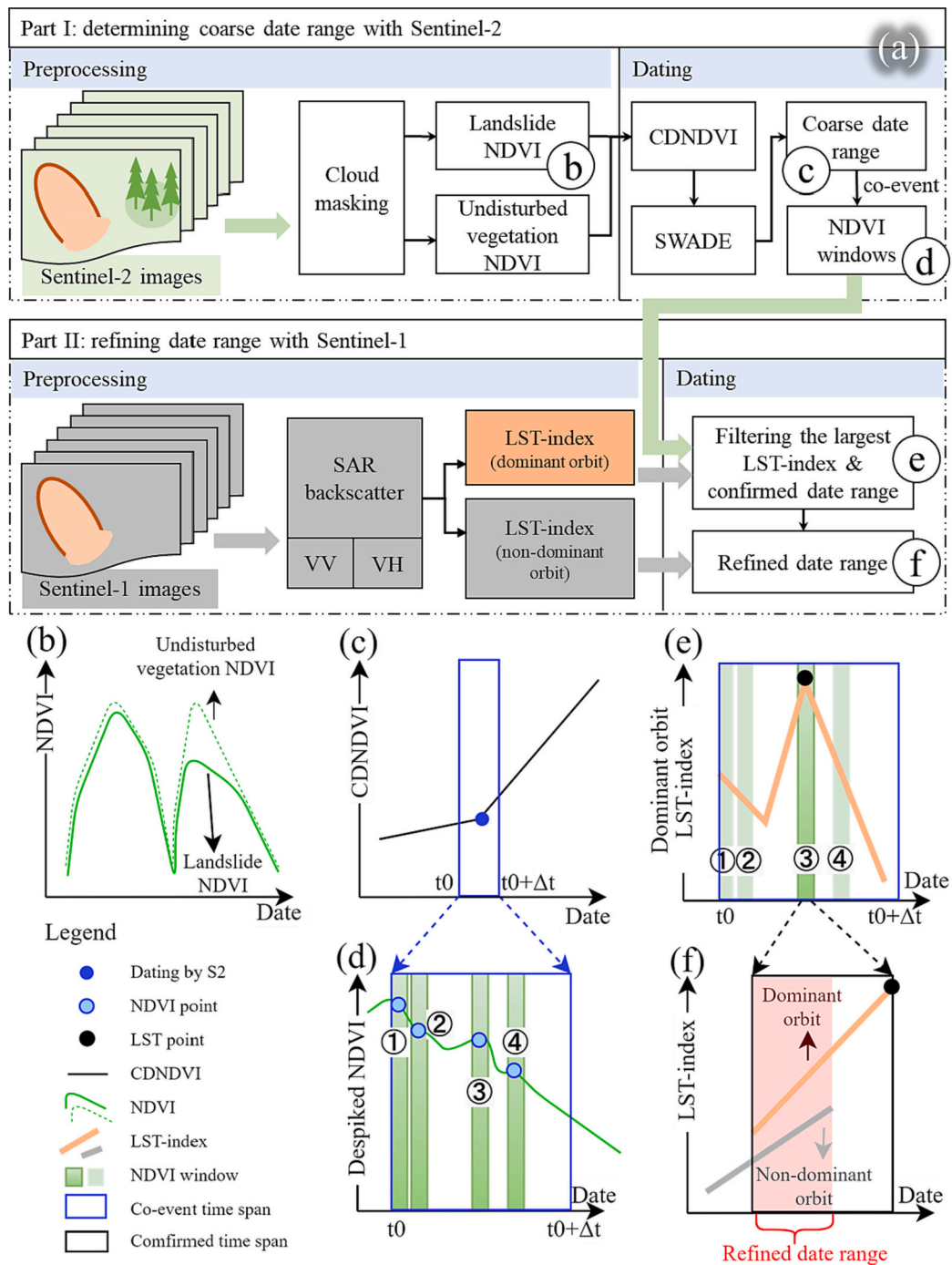
Fig. 1. Landslide dating framework using Sentinel-1 and -2 conceptually illustrating the processing steps (a). Panels (b)-(f) conceptually illustrate the data for some of the steps in the upper part of the image. In part I of our workflow, NDVI (Normalized Difference Vegetation Index) time series of landslide and vegetation (b) are collected from Sentinel-2 imagery. By comparing these time series a coarse landslide date range (c) is generated through CDNDVI (cumulative difference between vegetated NDVI and landslide NDVI) time series by the SWADE (Segmented Wavelet-Denoising and stepwise linear fitting) method (Fu et al., 2023). Next, a 6 month "co-event" is selected around the coarse date range for which we select the sudden decreases in NDVI as potential landslide occurrences (we select a maximum of five, in the illustration above four potential landslide dates are identified – see panel d). In part II, both VV and VH backscatter are acquired from Sentinel-1, and are used to obtain the most likely detailed landslide date range using the LST-index (landslide dating index) which quantifies the change in backscatter over time (e), and attain the final refined date range (pink bar) (f) when non-dominant LST-index time series is overlapped with dominant LST-index time series, and their overlapping provides shorter date range of landslide. (For interpretation of the references to colour in this figure legend, the reader is referred to the web version of this article.)

2.1. Dating part I: Determining a coarse date range with Sentinel-2

2.1.1. Preprocessing of Sentinel-2 data

We have used the Sentinel-2 Level-1C data because more Level-1C than Level-2A images are available in the GEE archive. A cloud mask algorithm (maskS2clouds, provided by GEE) was applied to the Quality Indicators for cirrus and clouds in Sentinel-2 to exclude images with high cloud coverage. Cloud masking introduces some uncertainty in the dating framework because pixels are masked out from the images. To minimize the effects of masked pixels deteriorating the temporal trends of the NDVI, we set the cloud threshold in such way that images were only included if <30% of the landslide area was masked out (i.e., >70%

is visible).

For all remaining Sentinel-2 images the NDVI was computed to assess vegetation cover and to assess sudden changes of vegetation cover in the time series of images. NDVI was computed as:

$$NDVI = (NIR - RED)/(NIR + RED) \qquad (1)$$

It remains challenging to assess vegetation cover, and abrupt changes of cover, by the NDVI for such variety of landslides because both pre- and post-NDVI vary among different kinds of plant or tree species and due to seasonality. We compensate for seasonality and for species variation of the NDVI values by comparing NDVI values in a polygon directly upon the landslide with NDVI values in a polygon with undisturbed vegetation directly adjacent to the landslide. Natural factors such as annual growth and increase of vegetation cover, that might impact the dating framework, are corrected for by detrending the NDVI values in the undisturbed vegetation polygons. When sudden anomalies of the NDVI are present, they are most likely caused by landslide events. Furthermore, we denoised both the landslide and the undisturbed NDVI time series by applying a 'movemean' algorithm with a sliding window of 7 images to ensure outliers related to undetected clouds were excluded from further analysis (Fig. 1b).

2.1.2. Dating using Sentinel-2 imagery

We perform an initial dating estimate using optical Sentinel-2 imagery using the SWADE method, previously published by Fu et al., (2023). The concept of the SWADE method is to detect landslide-induced vegetation disturbance by comparing NDVI values on the landslide with NDVI values of the undisturbed vegetation adjacent to the landslide. SWADE compares the time series of undisturbed NDVI and landslide NDVI, and generates the cumulative difference between the undisturbed NDVI and landslide NDVI (CDNDVI, Fig. 2), defined as:

$$CDNDVI = \sum_{t=1}^{t=T}(\Delta NDVI)_t = \sum_{t=1}^{t=T}(NDVI_V - NDVI_L)_t \qquad (2)$$

where ΔNDVI is the difference between the undisturbed NDVI and landslide NDVI. $NDVI_L$ and $NDVI_V$ are mean NDVI values in the landslide zone and undisturbed vegetation zone per selected image, respectively. The t is timestep and the T is the time range.

Fig. 2 shows the three different main patterns of NDVI and CDNDVI development over time. Pattern I shows the same vegetation growth rate in the pre-landslide zone as in the reference vegetation zone, but less vegetation in the post-landslide zone. Pattern II shows less vegetation in the pre-landslide zone compared to the reference vegetation zone, and less vegetation in the post-landslide zone. Pattern III indicates more

vegetation in the pre-landslide zone than in the reference vegetation zone, but relatively more vegetation in the post-landslide zone than other two patterns. The CDNDVI computes the cumulative differences of landslide NDVI and undisturbed vegetation NDVI values and hence, it enhances the difference between the landslide area and the reference area of undisturbed vegetation (Fig. 2c). Even if the post-landslide NDVI decrease is very small, e.g. around 0.1, the slope break will still be clearly useful for identifying the landslide date and the pre- and post-landslide NDVI period (Fig. 1c). Overall, we identify the moment of landslide occurrence at the point where the slope of the CDNDVI curve in the post-landslide period is positive and larger than that in the pre-landslide period. If more than one point is detected, the post-landslide section with largest slope through CDNDVI will be chosen as the largest change point. The whole CDNDVI time series will be segmented in at least two segments, e.g., pre- and post-landslide period. The largest change point in the segmented CDNDVI time series that follows one of these three situations is then selected as the most probable landslide occurrence date range and first preliminary date assessment (Fig. 1c). For further details on the SWADE method we refer to Fu et al., (2023).

2.1.3. Selecting of an initial time window to study further using SAR

The next step in landslide dating is defining a temporal window around the largest change point of the CDNDVI-values (Fig. 1c,d). This window is required because the largest change point of CDNDVI in the time series might be affected by cloud cover and by the 'move-mean'algorithm. A time span of 6 months (Burrows et al., 2022) is defined around the largest change of CNDVI. In the next section we describe how this time gap is filled by Sentinel-1 observations to refine the landslide date. Then, we convert the original landslide NDVI to the despiked landslide NDVI values in this 6-month time span. This is done because the smoothed landslide NDVI time series might, after the 'movemean' algorithm, not contain the original NDVI values, especially the NDVI values just before and just after landslide occurrence (Fig. 1d). Despiking is based on the idea that the vegetation damaged or removed by the landslide will not completely recover within three months (i.e., the number of points in the later three months from which the NDVI is higher than that of the checked points should be <3). If the vegetation has recovered sooner, the drop in NDVI was probably caused by other factors (e.g., clouds), and we work with the smoothed, despiked, NDVI series; if this is not the case we work with the original, unsmoothed, NDVI series.

From the despiked NDVI time series we can now select all relevant NDVI time windows potentially associated with landslide occurrence.
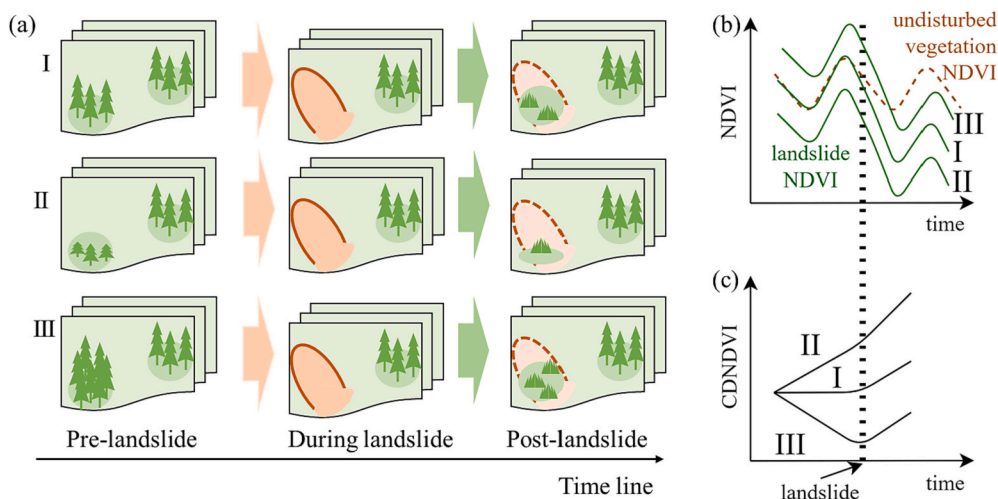

Fig. 2. The three main types of vegetation change patterns (I, II and III) before and after a landslide. (a) describes the vegetation mass changes over time; polygons of the landslide area and undisturbed vegetation area are used for the SWADE dating method. (b) shows NDVI time series of undisturbed vegetation and landslide. (c) shows CDNDVI time series.

We define these as time windows characterized by sudden decrease in NDVI. We extract a maximum of five NDVI windows. The width of the windows is defined by the date of the pre- and post-images (Fig. 1 I, d). Hereafter Sentinel-1 data is used for each time window to narrow down the landslide occurrence date. This allows to remove false positive NDVI decrease events and to identify the most probable landslide occurrence date (Fig. 1 II, e).

2.2. Dating part II: Refining the date range with Sentinel-1

The Sentinel-1 system transmits microwave signals in the C-band (~5.6 cm) towards the earth surface and registers the reflected / backscatter signal. The SAR sensor is observing the earth surface in west-looking direction during descending mode (north-south) and east-looking direction during ascending mode (south-north). Sentinel-1 transmits and receives the microwave signal in horizontal or vertical polarization, resulting in two bands of VH and VV in the Interferometric Wide (IW) swath. During image acquisition the look angle varies as a function of flight altitude while looking at the same object at the surface. Here we used time series of Sentinel-1 SAR C-band images from various flight altitudes and in VV and VH mode due to coverage imbalance of Sentinel-1 backscatter.

When a landslide occurs, slope steepness, surface roughness and sometimes slope aspect change, are altering the SAR backscatter (Burrows et al., 2022; Zhu et al., 2021). Compared to optical images, interpretation of radar images is challenging – for example when comparing histograms (Fig. 3a-d). In addition, depending on whether the aspect of the satellite sensor in orbit is facing towards or facing away from the landslide, an increase or decrease in the VH and VV backscatter is possible (Fig. 3e, f). Therefore, to account for these effects we compute a change vector index (Chen et al., 2003; Wang et al., 2022) to the SAR data amplitude summing up all backscatter changes for the pixels inside the landslide polygon (we refer to this change vector as the LST-index from hereon to indicate LandSlide datTing index). We then assume that the date of landslide occurrence corresponds to the maximum change in backscatter.

2.2.1. Preprocessing of Sentinel-1 data

The Sentinel-1 SAR backscatter signal received from a landslide area is a function of sensor properties and terrain properties (Fig. 4a). The descending and ascending mode usually provide a clear view of the exposed side of a mountain or hill, leaning towards the sensor, while layover or shadow image effects will occur when the slope is oriented away from the sensor. Although the SAR images in the archives are
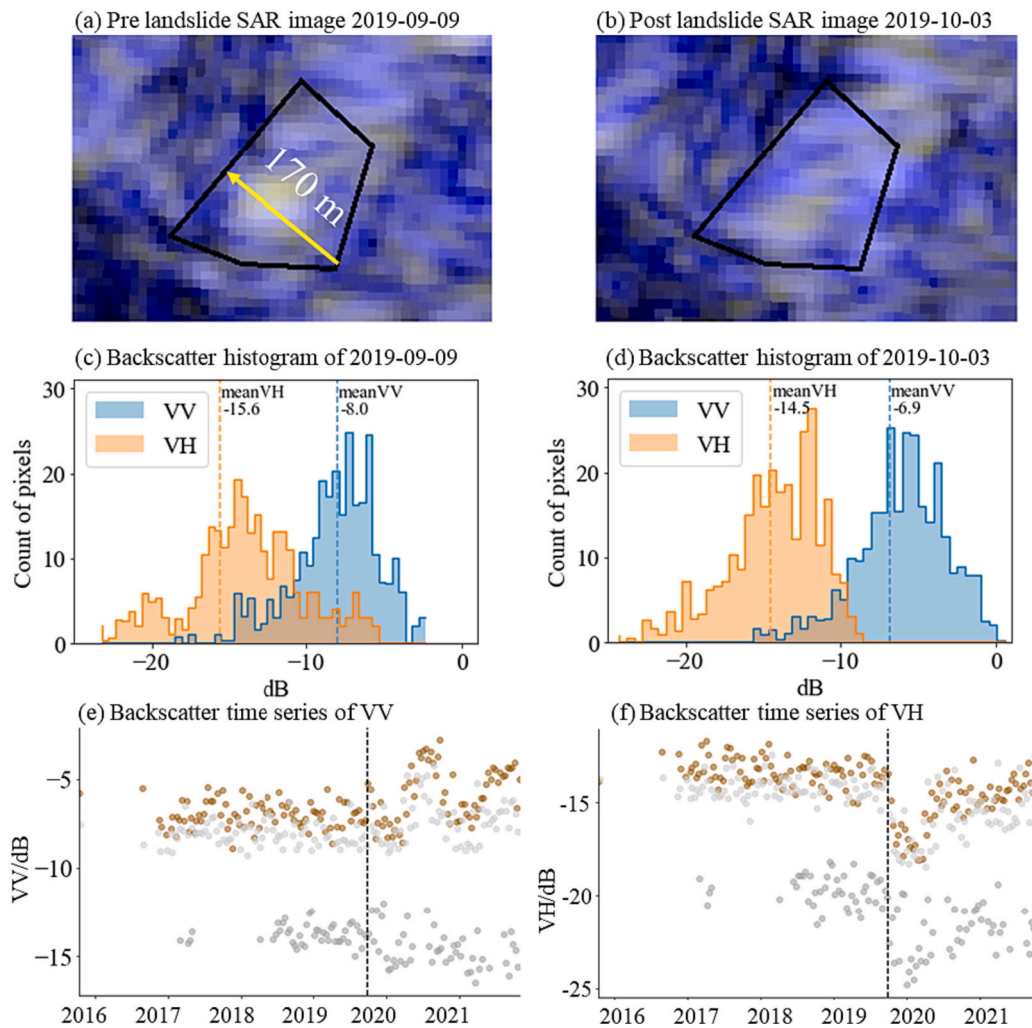

Fig. 3. Sentinel-1 SAR images before (a) and after (b) the occurrence of landslide and their VH and VV backscatter in RGB colors (red: VH, green: VH, blue: VV). Due to the visual similarity of the two SAR images, the corresponding numerical histograms of pre- and post- landslide backscatter values given in panel (c) and (d) are needed to identify the surface changes. Panels (e) and (f) are mean backscatter time series of VV and VH, respectively over the landslide polygon; the dashed vertical line denotes the landslide occurrence date – highlighting that the landslide is especially picked up by the VH backscatter signal. (For interpretation of the references to colour in this figure legend, the reader is referred to the web version of this article.)
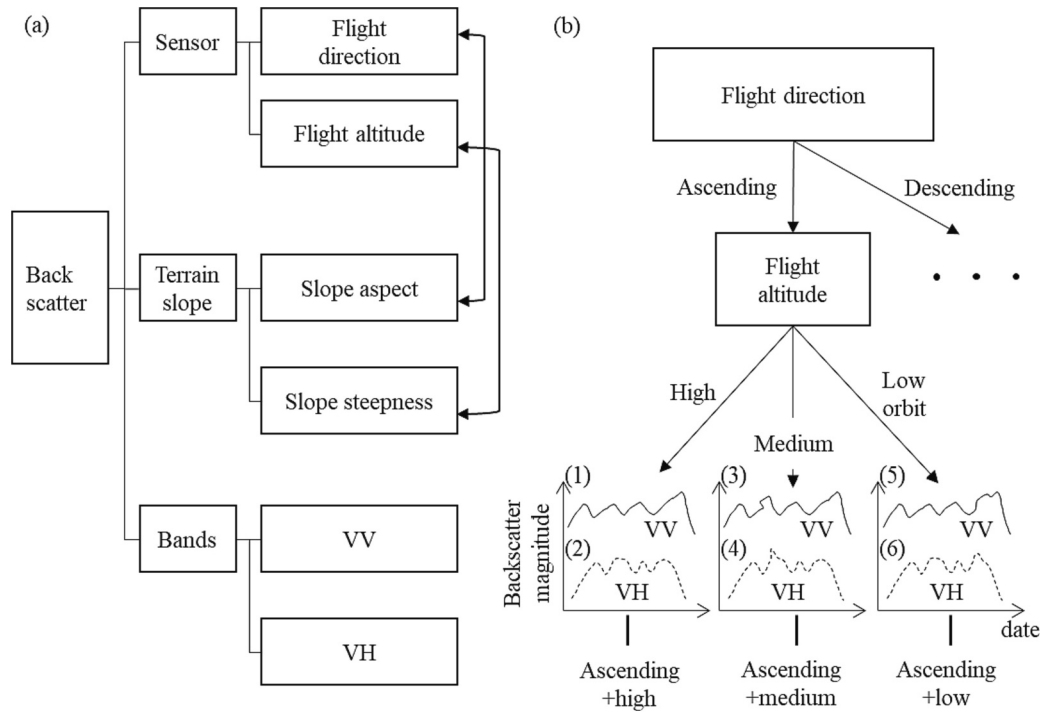
Fig. 4. Sentinel-1 SAR signal influenced by sensor, terrain and bands (a), and (b) data processing to separate backscatter time series according to the flight direction, flight altitude and polarization bands, resulting in six time series of backscatter magnitude for the ascending mode.

'terrain corrected' by the European Space Agency, the amplitude of backscatter from a landslide will still vary between descending and ascending mode. The operation altitude and look angle of a Sentinel-1 satellite varies with orbit number resulting in different backscatter values for the same surface areas. Additionally, the aspect and steepness of landslides and slopes in general are important terrain properties for backscatter. The aspect affects SAR backscatter similar to the satellite overpass mode (descending or ascending), while the slope steepness has a similar effect as the look angles (or flight altitude). Considering the above, we not only separate descending and ascending mode into different time series, but also discriminate different overpass orbit numbers into different time series when refining the landslide date range using Sentinel-1. Finally, we select and analyze several different SAR time series (Fig. 4b).

Next, we compute the "LST-index" from the SAR images to refine landslide dating. The LST-index is calculated in three different ways, using the VV signal, the VH signal, and a combination of VV and VH, because VV and VH interact differently with ground surface properties (Henderson and Lewis, 1998):

$$LST(VV)_t = \frac{\sum_1^n (VV_t - VV_{t-1})^2}{n} \tag{3}$$

$$LST(VH)_t = \frac{\sum_1^n (VH_t - VH_{t-1})^2}{n} \tag{4}$$

$$LST(VV + VH)_t = LST(VV)_t + LST(VH)_t \tag{5}$$

Herein, n is the number of pixels within the polygon area and t is time of image acquisition.

2.2.2. Dating using Sentinel-1

Changes in the SAR backscatter time series may result from various factors such as vegetation seasonality, snowfall, moisture conditions and in our case landslide occurrence, making it difficult to confirm whether the landslide caused the change in backscatter. Within our landslide dating framework, we aim at determining the date of landslide

occurrence within the pre-selected NDVI windows as described in section 2.1.3 by finding the strongest terrain change expressed by our LST-index.

To obtain the best date estimate we first select the pass orbit with the highest averaged backscatter values. We refer to this orbit as the 'dominant orbit', and we select this orbit for further evaluation of the LST-index. The largest LST-index value from the dominant pass orbit within the pre-defined NDVI windows is then selected as the most likely date of landslide occurrence (Fig. 1e, f). As a result, a final date range of landslide occurrence can be estimated, corresponding to the dates of the nearest pre- and post-event Sentinel-1 image (Fig. 1f).

2.3. Landslide validation dataset

All the 60 landslides are selected from recently published journal papers or news items (Fig. 5 and Supplementary Materials). The oldest landslide in our database occurred on 2016-09-28 and the most recent landslide on 2021-08-13. The geometric characteristics of the landslides vary substantially, with areas ranging from 10^4 m^2 to 8.75×10^5 m^2, and displaced volumes from 3×10^3 m^3 to 4.26×10^6 m^3. Unfortunately, surface areas or displaced volumes of the landslides are not reported for all landslides. The landslides are spatially delineated by drawing polygons by visual interpretation based on the published geographical information and based on observable landslide scars on Google Earth and Sentinel-2 images. Surface areas range from 1109 m^2 to 1.19×10^6 m^2 (Table S1 in Supplementary Materials). In total, 72% of the landslides were induced by precipitation, 5% of the landslides by earthquakes, 13% of landslides by other factors (i.e., geologic fracturing, engineering constructions), and the remaining 12% of the landslides are triggered by unknown factors. All selected landslides have resulted in vegetation cover decrease as well as terrain deformation, which makes them theoretically suitable for detection from satellite images.

2.4. Temporal accuracy and uncertainty

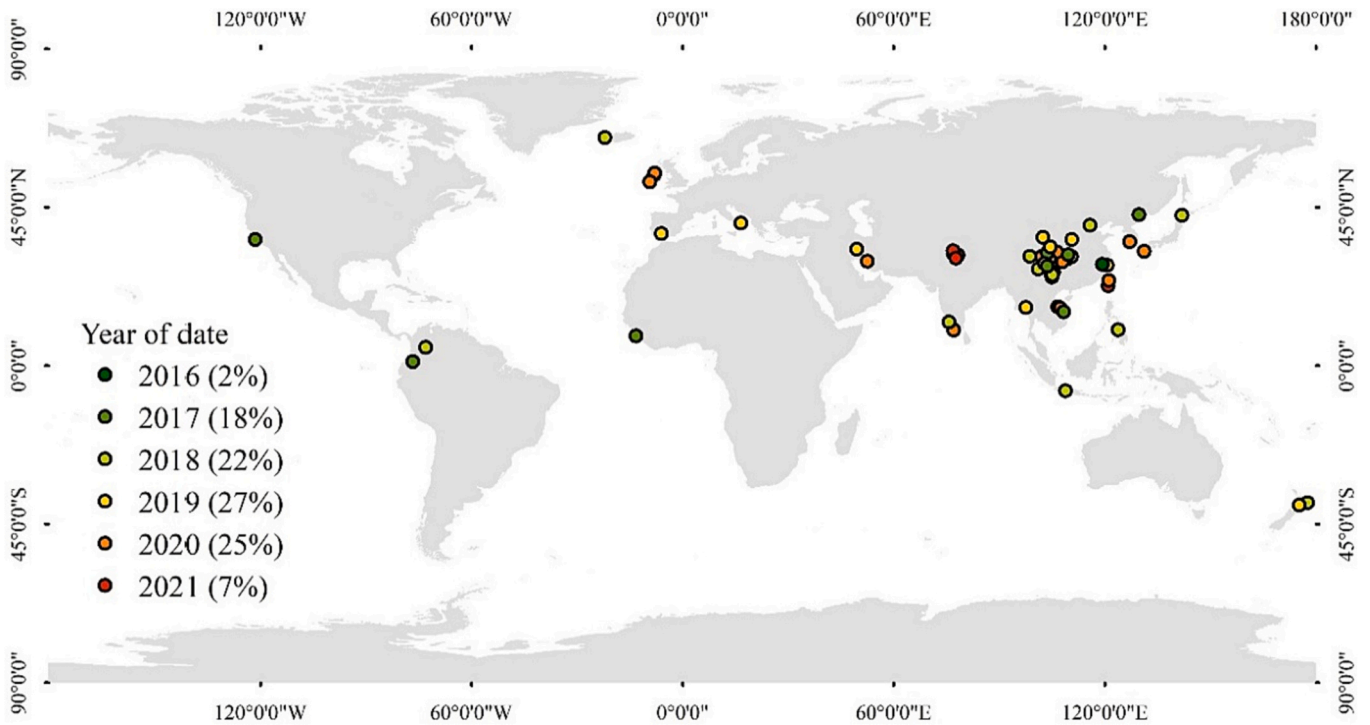To evaluate whether the combination of optical and SAR imagery

Fig. 5. Spatial distribution of the 60 studied landslides. The points indicate the location and year of occurence of the landslides. The number in brackets indicates the percentage of the landslides that occurred in a specific year.

outperforms landslide dating by only optical imagery, and how the use of VV or VH affects the landslide dating performance, four different landslide dating results are given: S2 only (only using Sentinel-2), S1/2 VV (Sentinel-1/2 combination using VV), S1/2 VH (Sentinel-1/2 combination only using VH), S1/2 VV + VH (Sentinel-1/2 combination using both VV and VH). To quantify the accuracy of each of the four approaches we adapted the time lag and uncertainty range by following the method of Reiche et al. (2018a) (Fig. 6). Time lag is defined as the date difference between the actual landslide date and the mean date based on estimated pre- and post- image acquisition date. Then, we

quantify the uncertainty range as the time difference between the actual landslide date and estimated pre- post-image date, respectively (Fig. 6). Related to the uncertainty range, we also generate the precision to determine how large the gap is between estimated pre- and post-image dates.

3. Results

In this section, we first provide an example of landslide dating with our landslide dating framework (section 3.1). Then we evaluate the
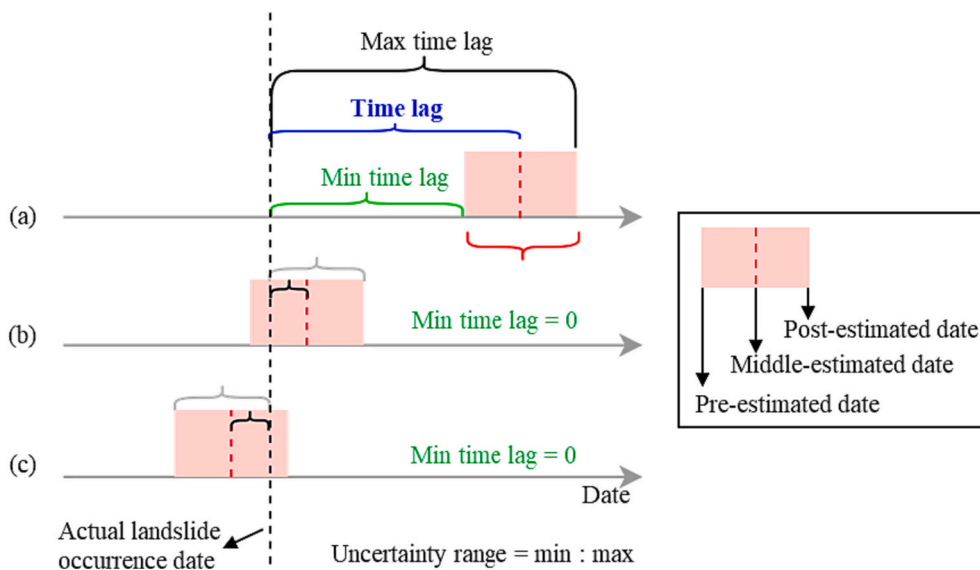

Fig. 6. Accuracy assessment to evaluate landslide dating. Time lag (black curly brackets) is the date difference between actual landslide occurrence date (black dashed line) and estimated middle date (red dashed line) of estimated date range (pink box). The max and min of time lag are shown as black and green curly brackets, respectively, showing uncertainty of landslide dating results. The precision is shown by the red curly bracket, defined as the time period between the pre- and post-images. (For interpretation of the references to colour in this figure legend, the reader is referred to the web version of this article.)

overall dating accuracy for the 60 studied landslides (section 3.2). Finally, we analyze how landslide area affects dating accuracy (section 3.3).

3.1. Example of landslide dating combining optical and SAR imagery

The process of dating the TeOreOre landslide, which occurred on 2019-10-02 in New Zealand, using a combination of optical and SAR imagery is illustrated in Fig. 7. By using the SWADE approach, the CDNDVI in Sentinel-2 imagery (Fig. 7a) estimates that the landslide occurrence was between 2019 and 09-26 and 2019-09-28, which is a narrow date range slightly earlier than the real landslide date (Fig. 7b). Based on this date range, a 6 month 'co-event' time series is generated (Fig. 7b), wherein we analyze the despiked landslide NDVI time series. Within the co-event time series, three NDVI windows with strongly decreasing NDVI values are considered probable landslide date ranges (Fig. 7c). Within these three periods we then define a definitive date range using the SAR data collection. Sentinel-1 SAR data records earth observations in different orbit passes (different flight direction and altitude of Sentinel-1 satellite). We select the dominant orbit pass based on the largest averaged backscatter (Fig. 7d). The backscatter from this dominant orbit pass is then transformed into a LST-index time series (Fig. 7e). We then identify the dating of landslide occurrence by identifying the pre- and post-image around the maximum LST-index value within the three pre-defined NDVI windows. This definition determines the most likely date range of landslide occurrence, but also enables us to exclude the other false positive NDVI windows (Fig. 7f). In this example, landslide occurrence date range is determined at 2019-09-26 to 2019-10-03 by S1/2 VV, correctly capturing the real landslide occurrence date (Fig. 7f and Table 1).

Fig. 8 illustrates the reason for generating three NDVI windows with a substantially decreasing NDVI for the TeOreOre landslide, wherein we

Table 1
Landslide dating accuracy for the TeOreOre landslide.

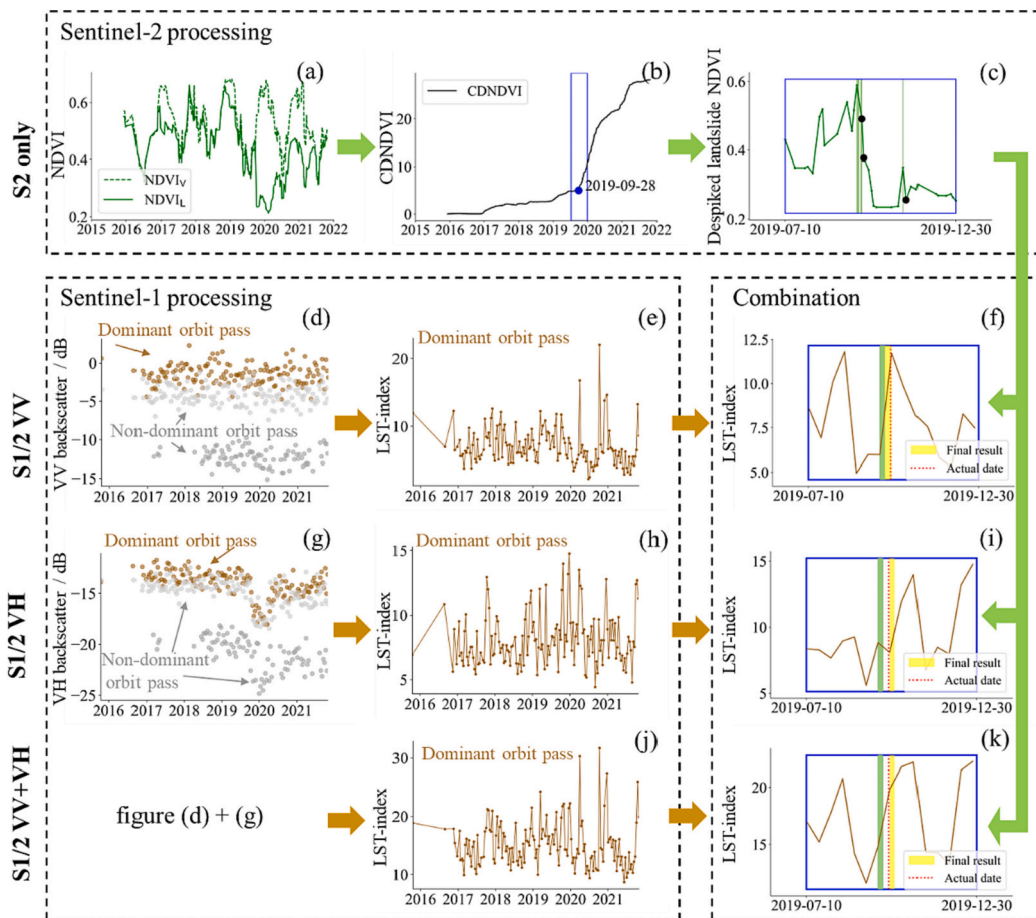| Different results	S2 only	S1/2 VV	S1/2 VH	S1/2 VV + VH
Pre estimated date	2019-09-26	2019-09-26	2019-10-03	2019-10-03
post estimated date	2019-09-28	2019-10-03	2019-10-08	2019-10-08
Min /day	3.1	1.3	1.3	1.3
Time lag /day	4.1	2.0	3.8	3.8
Max /day	5.1	5.3	6.3	6.3
Uncertainty range / day	3.1–5.1	1.3–5.3	1.3–6.3	1.3–6.3
Precision /day	2.0	6.6	5.0	5.0

Fig. 7. Landslide dating workflow for the TeOreOre landslide that occurred on 2019-10-02. For the Sentinel-2 processing, (a) shows NDVI time series of the referenced undisturbed forest zone (green dashed line) and the landslide zone (green solid line); (b) is the CDNDVI time series, together with the probable post-landslide date (blue point; the landslide dating result by S2 only) and the co-event 6 month period (blue rectangle); and (c) is the despiked landslide NDVI with three NDVI windows of potential occurrence (green bars), and in (c) the black points marked the post-image date of each NDVI window. (d) shows VV backscatter time series of all orbit passes, wherein we define the dominant orbit pass based on the highest mean average backscatter. (e) shows LST-index time series by VV. (f) shows the landslide dating result of S1/2 VV, with LST-index time series (brown solid line), true positive NDVI window (green bar), final date range (yellow bar) and actual landslide occurrence date (vertical dashed line). Similarly, (g, h, i) and (j, k) show the landslide dating results of S1/2 VH and S1/2 VV + VH, respectively. (For interpretation of the references to colour in this figure legend, the reader is referred to the web version of this article.)
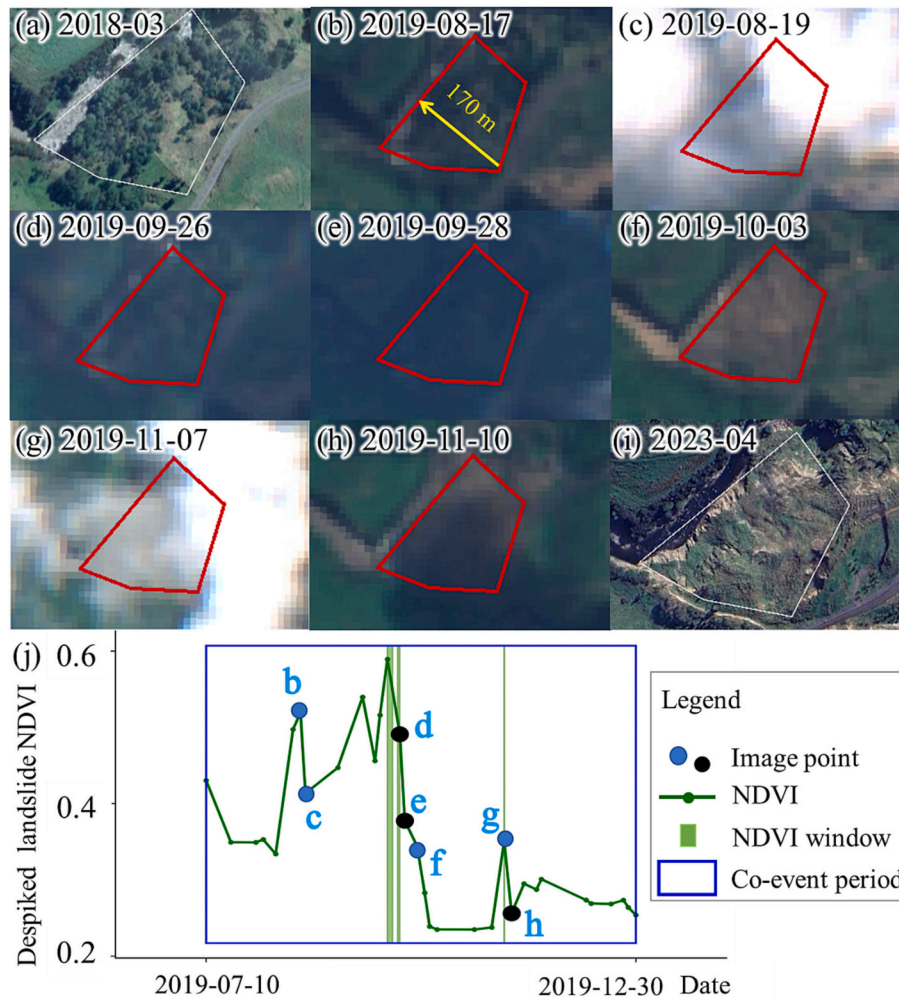
Fig. 8. Pre- (a) and post- (i) landslide Google earth images of TeOreOre landslide; and pre- (b-e) and post- (f-h) landslide Sentinel-2 images of TeOreOre landslide with their NDVI values along the despiked landslide NDVI (j). Images and points of d, e and h are the post dates of three NDVI windows, respectively. (a) The yellow arrow shows landslide movement direction and distance; white and red polylines show the landslide extent. (For interpretation of the references to colour in this figure legend, the reader is referred to the web version of this article.)

later define the landslide date range based on the maximum change in SAR backscatter defined by the LST-index. The image of Fig. 8c shows a NDVI decrease (in Fig. 8j) as a result of clouds, cirrus or cloud shadow, and it can easily be filtered out because the changes in NDVI values occur over a short period only (<3 months). However, the three remaining NDVI windows (Fig. 8j) all show a longer period of decreasing NDVI values without rapid recovery and may therefore still represent landslide occurrence, but two of those are false positives as a result of cirrus clouds (Fig. 8d, e) and cloud shadows (Fig. 8h). These false positives are later removed by analyzing the LST-index. This example illustrates how combining analyses of optical satellite images with SAR imagery can remove false positive NDVI windows as a result of cloud and cloud shadow effects, and thereby increase date accuracy (Fig. 7).

3.2. Overall landslide dating accuracy

Fig. 9 displays and compares the results of the different landslide dating approaches tested here (Table S2 in Supplementary Materials). Overall, all the estimated landslide occurrence dates are well-correlated. The R-squared values of S1/2 VV + VH and S1/2 VV are both larger than that of S1/2 VH and S2 only. The root mean squared error of S1/2 VV is similar to that of S1/2 VV + VH, both of which are lower than that of S1/2 VH and S2 only.

For the overall temporal accuracy assessment, the average time lag of

landslide dating is 51 days by S2 only (Fig. 10). Combining SAR and optical imagery leads in this case to a pronounced improvement of dating accuracy, e.g., time lag and precision. Sentinel-1/2 using the VV band yields an average time lag of 26 days while using the VH band results in a larger average time lag of 34 days (Fig. 10). The lowest time lag of 23 days was acquired by using S1/2 VV + VH. The uncertainty range is defined by the min and max time lag. The uncertainty range of S2 only is from 42 to 60 days. For S1/2 VV + VH, the uncertainty range is from 20 to 27 days. The higher uncertainties in the landslide dating results using optical Sentinel-2 images only are mainly due to the presence of cloudy images around the time of landslide occurrence, leading to limited availability of uncontaminated images. The precision of landslide dating using S2 only is 18 days, which is higher than the dating using S1/2 with an precision of 8 days.

3.3. Importance of area for dating accuracy

Fig. 11 shows the effect of landslide area on detection accuracy. We find that 85% out of 13 landslides with an area larger than $20 \times 10^4 \, \text{m}^2$ is dated within 7 days accuracy using S1/2 VV. With a relaxation of temporal accuracy, larger percentages of successfully detected landslides are obtained. Within 0–90 days' accuracy, the results of S1/2 VV and S1/2 VV + VH reach 100% accuracy when detecting landslides with an area larger than $20 \times 10^4 \, \text{m}^2$; the percentages of all four tested
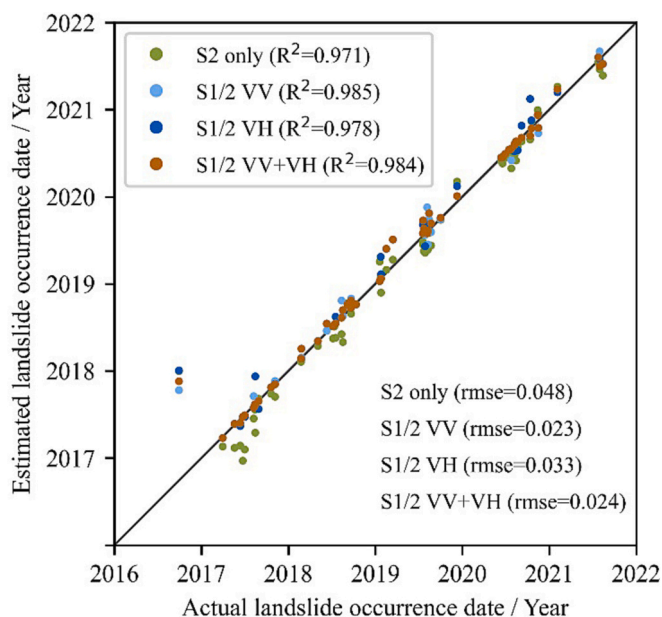
Fig. 9. Comparison of the estimated and actual landslide occurrence dates, highlighting R-squared (R^2) and root mean squared error (rmse). S2 only (only using Sentinel-2), S1/2 VV (Sentinel-1/2 combination using VV), S1/2 VH (Sentinel-1/2 combination only using VH), S1/2 VV + VH (Sentinel-1/2 combination using both VV and VH).

Fig. 10. Boxplots of landslide dating accuracy distribution among S2 only (only using Sentinel-2), S1/2 VV (Sentinel-1/2 combination using VV), S1/2 VH (Sentinel-1/2 combination only using VH), S1/2 VV + VH (Sentinel-1/2 combination using both VV and VH). The min, time lag and max have been explained in the section 2.4. Note that the median is typically much smaller than the mean for all detection methods.

landslide dating methods are >84%. For smaller landslides with an area $<3 \times 10^4$ m^2, the accuracy percentages of all four landslide dating results ranges between 5–50% for an accuracy of 0–7 days, making it difficult to achieve highly accurate landslide dating. For the same temporal accuracy, the detection percentages range between 38–85% for landslides with an area larger than 20×10^4 m^2. To compare the performance of landslide dating using optical imagery only, to using both optical and SAR imagery, Fig. 11 illustrates that the performance of all three landslide dating results using S1/2 are significantly better than the result of landslide dating using S2 only, in all the area categories.

4. Discussion

The characteristics of land cover changes can be captured by optical and radar remote sensing satellites (Mullissa et al., 2021) and this yields valuable data to natural hazard monitoring studies. To monitor landslides, on the one hand, optical remote sensing images mainly describe the spectral reflectance variations of land cover on the landslide body (Deijns et al., 2022; Wang et al., 2022); while on the other hand, radar remote sensing images provide backscatter information on land cover and terrain roughness changes (Burrows et al., 2022; Meng et al., 2022). NDVI values derived from optical remote sensing images can indicate vegetation removal by landslide activity, but NDVI values are often negatively affected by clouds and poor weather during and around the time of landslide activity. Conversely, backscatter observations derived from SAR remote sensing images are cloud and weather-insensitive but variations in the backscatter signal might be caused by various factors other than landslides (Burrows et al., 2022; Deijns et al., 2022). Taking advantage of the merits of both optical and SAR satellite imagery, we have proposed a landslide dating framework here to date landslides using land cover disturbance based on sudden changes in NDVI values in optical imagery and large terrain changes observed in SAR imagery. Our method processes, analyses and applies the SWADE method (Fu et al., 2023) together with Sentinel-2 imagery. We supplement this method with SAR image analysis using the LST-index that quantifies maximum backscatter change in the SAR time series.

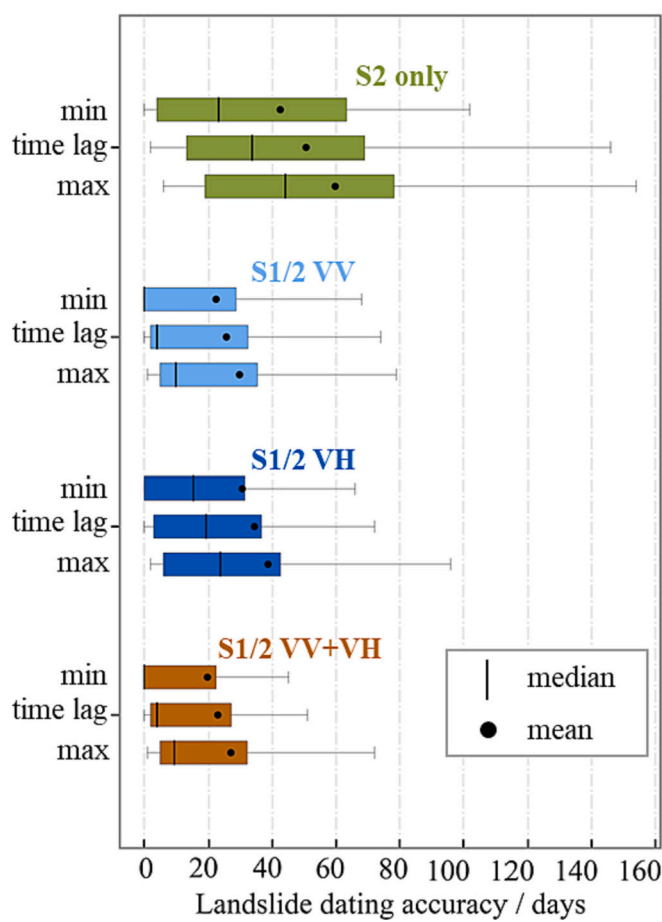Below, we compare the accuracy of our landslide dating framework

to previous landslide dating work (section 4.1), after which we discuss factors that affect the accuracy of our framework (section 4.2). We end by discussing the practical applications of our new dating framework (section 4.3).

4.1. Dating accuracy relative to previously published methods

We selected from literature four landslide dating studies using optical or SAR satellite imagery, and we used their reported accuracies to compare with our results here (Burrows et al., 2022; Deijns et al., 2022, 2020; Fu et al., 2023). Landsat satellites have been observing the earth for >40 years since the 1980s and this time series is available and used to date landslides. Two of these four studies used Landsat imagery derived NDVI time series, and applied them successfully for (semi-)automatic landslide dating of 66-landslides in the Buckinghorse River area in Canada (Deijns et al., 2020; Fu et al., 2023). The 16-day revisit frequency and 30 m spatial resolution of Landsat satellite images resulted in an accuracy ranging from a few weeks to over two years (Deijns et al., 2020). In contrast, our landslide dating framework achieves more accurate date detections with a mean accuracy of 51 days when only using optical images. We primarily attribute this higher accuracy to the high spatial resolution and high revisit frequency of Sentinel-2 satellites.

SAR amplitude techniques for landslide dating have been developed using Sentinel-1 image time series by Burrows et al. (2022) and Deijns
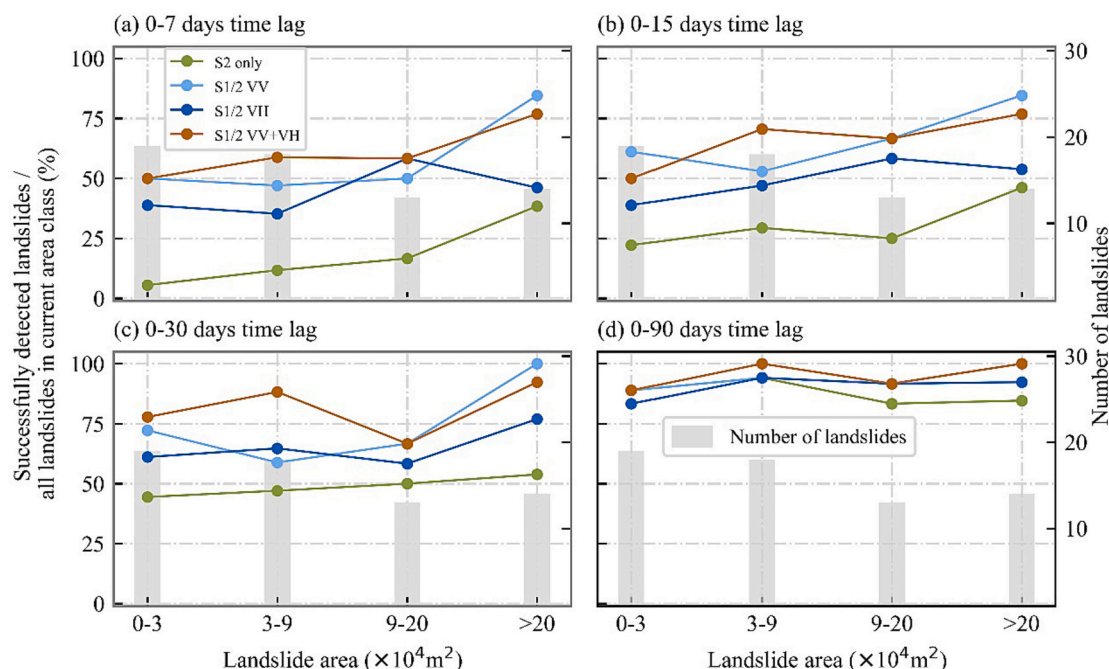
Fig. 11. Percentages of successfully detected landslides in different categories of landslide area for a (a) 0–7 days time lag, (b) 0–15 days time lag, (c) 0–30 days time lag and (d) 0–90 days time lag. The number of landslides is shown on the right y-axis.

et al. (2022). A major complication for dating landslides using SAR imagery, is that landslide activity may both induce an increase or decrease of backscatter coefficients due to contrasting terrain changes (Burrows et al., 2022). In the work of Burrows et al., (2022) three backscatter characteristics are used for the landslide dating: landslide - background differences, pixel variability and geometric shadows. By applying SAR processing and landslide identification, their dating methods have been evaluated on three inventories of rainfall-induced landslides, and they finally detected the timing of 20%–30% of all landslides with an accuracy of 80%. This relatively low accuracy is caused by a number of processes other than landslides causing land deformation according to their study (e.g., snowfall or snowmelt, vegetation changes, soil moisture changes or human activity). Deijns et al., (2022) used Sentinel-1 SAR images to date landslides and flash floods in the East African Rift. They achieved maximum dating accuracies ranging between 1 and 47 days, employing trends in coherence and detrended coherence for detection. However, their dating approach is not only targeted on landslides, but also on flood hazards. The backscatter for the water body behaves distinctly different compared to non-water ground objects (Henderson and Lewis, 1998). Comparatively, the landslide dating framework in our study performs better, likely because we focus on landslides only and optimally combine data from optical and SAR satellites.

Similar to landslide temporal detection, deforestation research also applies temporal detection on vegetation removal and land cover disturbance. Many of these deforestation detection studies provide valuable methods and references to landslide dating studies and are worth mentioning here. Fusion of Landsat and SAR analysis or SAR-only analysis have been applied to detect deforestation in the (sub-) tropical zones, achieving relatively high temporal accuracy of approximately one month (Reiche et al., 2018a, 2015). These studies obtained similar or even higher temporal accuracies than our study, but their methods are not directly suitable for landslide dating because no severe terrain slope changes occurred after deforestation, while this typically happens after landslide occurrence. SAR backscatter from the ground will change considerably with altering slope steepness and roughness after slope failure compared to just forest removal. Slope altering and changing surface roughness generally cause the backscatter amplitude of some

parts of the landslide body to increase while other areas will decrease, hampering the identification of the landslide activity (Burrows et al., 2022; Mondini et al., 2021). A recently introduced mowing detection study combining Sentinel-1 and Sentinel-2 might also not be applicable to landslide dating because the method aims at detecting sudden backscatter coefficient increases while landslides cause far more complex backscatter change patterns (De Vroey et al., 2022).

By comparing our and other previously published studies (Burrows et al., 2022; De Vroey et al., 2022; Deijns et al., 2022; Reiche et al., 2018a), it can be summarized that the backscatter coefficient of SAR images is easily affected by terrestrial slope settings and other processes such as snowfall and -melt and gradual vegetation growth. Therefore, we advocate that the presented landslide dating framework of first analyzing optical imagery and subsequently refining the time period using SAR imagery is a robust way of dating landslides on the basis of satellite imagery.

4.2. Factors affecting dating accuracy

Vegetation growth and cover is affected by the vegetation species, seasonality and climate zone. Vegetation developments are different around the world, making it difficult to define a standard threshold for NDVI decrease to date a landslide. In order to account for vegetation growth, vegetation seasonal cycles and vegetation development in different climate zones around the world within landslide dating methods, two approaches are viable. The first option is applying sinusoid and harmonic modelling as reported by Deijns et al. (2020) and Reiche et al. (2018b), which is used to follow and fit the vegetation growth by a sinusoidal cycle of forest in temperate or boreal climates. The fitting parameters of this mathematical model however result in a large variation for the different climate zones (e.g., (sub-)tropical, boreal, continental, or oceanic zones). Such an approach is laborious and time consuming, and would require local calibration and validation. The alternative, applied here, is selecting an undisturbed vegetation zone nearby but outside the landslide zone with similar vegetation characteristics (Burrows et al., 2022; Deijns et al., 2020). Such an approach is easy to implement and universally applicable, and its interpretation is straightforward and practical.

Our study indicates that the backscatter of VV responding to the vegetation and slope change is more sensitive than that of VH. Wu (1984) found likewise that land cover types are better delineated by multipolarization (HH, HV, and VV) than by single polarization (HH) transmitted and received by the X-band SAR. The landslide dating study that used SAR data (Burrows et al., 2022) obtained better results with VV than with VH using the C-band Sentinel-1 satellite. With respect to polarization comparison and application, our study suggests that the utilization and performance of SAR polarization modes depend on the specific applications and different settings of the SAR sensors.

Landslides cause changes in slope aspect and slope steepness, resulting in different SAR backscatter magnitudes before and after landsliding (Burrows et al., 2022; Zhu et al., 2021). Consequently, the dating of landslides with relatively large surface changes, for example resulting from vegetation removal or slope deformations, is easier than dating landslides with relatively small surface changes in SAR images. This is because more severe surface change is easier to detect in the SAR backscatter. To evaluate how land degradation affects landslide SAR backscatter, we need quantitative analyses where high resolution digital elevation models of pre- and post-landslide can be compared but such datasets are scarce. Knowledge on the impact of landslide slope geometry on SAR backscatter is very valuable knowledge and is recommended for future research and, if successful, could be included in our landslide dating framework.

Because of the high revisit frequency from optical satellite images and the use of the change vectors derived from SAR satellite images (LST-index), our landslide dating framework reaches an average overall accuracy of 23 days for the 60 landslides considered here. Our method does not accurately date three landslides in the available dataset and mismatching goes beyond 100 days. The oldest landslide in our dataset, the Suvillage rockslide (Ouyang et al., 2019), has a low accuracy due to the limited number of optical pre-landslide images. Only two pre-landslide images are available from the Sentinel-2 archive. This data limitation strongly decreases the landslide dating precision. Another illustrative case of low-accuracy dating is the Zaoling landslide (Cui et al., 2020). The landslide did not result in a decrease in NDVI values; conversely, an increasing NDVI of 0.03 followed and this leads to an incorrect detection of the date. The third low accuracy dating case is the Longjing landslide (Fan et al., 2019). For this landslide the LST-index value during actual landslide occurrence is not the highest within the NDVI window, possibly as a result of human engineering or secondary slope failure happening in the landslide zone. A similar sudden change in ground surface also occurred at the Mangapoike landslide (McGovern et al., 2021). The formation of a water pond at the landslide foot leads to a larger LST-index value after pond formation than during landslide occurrence, because the backscatter from the pond water is much lower than that from trees or bare ground. In short, data limitations and sudden ground changes unrelated to landslides can negatively affect the dating results.

4.3. Practical applications

This study shows that our landslide dating framework is capable of generating the date of landslide occurrence in various vegetation areas and for landslides resulting in vegetation decrease / removal and terrain deformation or change. By dating landslides for certain regions, landslide frequency-magnitude functions can be computed which are often key for landslide risk assessment and mitigation (Guzzetti et al., 2005). Knowledge of historical landslide development can furthermore be useful information for developing local landslide early warning systems (Mondini et al., 2021; Ouyang et al., 2019). In addition, accurately determining the date of occurrence of landslides might be helpful to identify the triggering mechanisms and conditions, e.g., local rainfall intensity-duration curves as landslide triggering mechanism (e.g., Guzzetti et al., 2008). By knowing the date range of landslide occurrence, one can track how landslides affect vegetation removal and recovery (Deijns et al., 2020; Qu et al., 2021). This is important information for ecological management, and for assessing landslide hazard and risk.

5. Conclusions

A landslide dating framework is proposed here which combines optical and SAR remote sensing satellite images. Firstly, we use NDVI time series from Sentinel-2 imagery to determine a rough potential landslide date range using the previously published SWADE (Segmented WAvelet-DEnoising and stepwise linear fitting) landslide dating approach. Less accurate dating, caused by cloud contamination and poor weather conditions, which is often the case when landslides occur, results in relatively large and sometimes false positive temporal windows of potential landslide occurrence. Therefore, we subsequently include and analyze cloud-insensitive SAR backscatter images, acquired by Sentinel-1, to remove false positive windows and refine the landslide date range using our landslide dating index (LST-index). This LST-index identifies and quantifies the magnitude of change in backscatter through time series, wherein we identify the date of landsliding as the largest change in backscatter. The feasibility and accuracy of our landslide dating framework is assessed using a 60-landslide dataset around the global / world.

Results show that the landslide dating framework has a pronounced accuracy increase when we complement optical image analyses with SAR backscatter analyses. The average overall accuracy of landslide dating, when only Sentinel-2 satellites imagery is used, is 51 days. This average overall accuracy is improved to 23 days when Sentinel-1 SAR satellite imagery is included in the analysis. In addition, our results suggest that the co-polarization backscatter is more sensitive to landsliding than cross-polarization backscatter, leading to more accurate landslide dating.

Our landslide dating framework can be utilized across various vegetated areas, and landslides can be dated if landslide activity causes sufficient vegetation cover decrease and land surface changes. The framework is suitable to constrain landslide occurrence date range within an accuracy of one month in most cases, by minimizing the influence of cloud cover, cirrus and cloud shadow. This work can provide a solid base for further landslide dating research, it provides a valuable tool for constructing landslide magnitude-frequency functions, and it helps determining the conditions triggering landslides by determining their date of occurrence, and contributes to the natural disaster early warning.

CRediT authorship contribution statement

Sheng Fu: Writing – review & editing, Writing – original draft, Visualization, Validation, Methodology, Funding acquisition, Formal analysis, Data curation, Conceptualization. **Steven M. de Jong:** Writing – review & editing, Writing – original draft, Supervision, Methodology, Conceptualization. **Xuejiao Hou:** Visualization, Conceptualization. **Job de Vries:** Writing – review & editing, Writing – original draft, Visualization. **Axel Deijns:** Writing – review & editing, Writing – original draft, Visualization. **Tjalling de Haas:** Writing – review & editing, Writing – original draft, Visualization, Supervision, Methodology, Conceptualization.

Acknowlegdements

Appendix A. Supplementary data

Supplementary data to this article can be found online at https://doi.org/10.1016/j.enggeo.2023.107388.

References

Akçar, N., Deline, P., Ivy-ochs, S., Alfimov, V., Hajdas, I., Kubik, P.W., Christl, M., Schlu, C., 2012. The AD 1717 rock avalanche deposits in the upper Ferret Valley (Italy): a dating approach with cosmogenic 10Be. J. Quat. Sci. 27, 383–392. https://doi.org/10.1002/jqs.1558.

Amatya, P., Kirschbaum, D., Stanley, T., Tanyas, H., 2021. Landslide mapping using object-based image analysis and open source tools. Eng. Geol. 282, 106000 https://doi.org/10.1016/j.enggeo.2021.106000.

Angeli, M.G., Pasuto, A., Silvano, S., 2000. A critical review of landslide monitoring experiences. Eng. Geol. 55, 133–147. https://doi.org/10.1016/S0013-7952(99)00122-2.

Behling, R., Roessner, S., Golovko, D., Kleinschmit, B., 2016. Derivation of long-term spatiotemporal landslide activity—a multi-sensor time series approach. Remote Sens. Environ. 186, 88–104. https://doi.org/10.1016/j.rse.2016.07.017.

Burrows, K., Marc, O., Remy, D., 2022. Using Sentinel-1 radar amplitude time series to constrain the timings of individual landslides : a step towards understanding the controls on monsoon-triggered landsliding. Nat. Hazards Earth Syst. Sci. 22, 2637–2653. https://doi.org/10.5194/nhess-22-2637-2022.

Casagli, N., Cigna, F., Bianchini, S., Hölbling, D., Füreder, P., Righini, G., Del Conte, S., Friedl, B., Schneiderbauer, S., Iasio, C., Vlcko, J., Greif, V., Proske, H., Granica, K., Falco, S., Lozzi, S., Mora, O., Arnaud, A., Novali, F., Bianchi, M., 2016. Landslide mapping and monitoring by using radar and optical remote sensing: examples from the EC-FP7 project SAFER. Remote Sens. Appl. Soc. Environ. 4, 92–108. https://doi.org/10.1016/j.rsase.2016.07.001.

Chen, J., Gong, P., He, C., Pu, R., Shi, P., 2003. Land-use/land-cover change detection using improved change-vector analysis. Photogramm. Eng. Remote. Sens. 69, 369–379. https://doi.org/10.14358/PERS.69.4.369.

Cossart, E., Braucher, R., Fort, M., Bourlès, D.L., Carcaillet, J., 2008. Slope instability in relation to glacial debuttressing in alpine areas (Upper Durance catchment, southeastern France): evidence from field data and 10Be cosmic ray exposure ages. Geomorphology 95, 3–26. https://doi.org/10.1016/J.GEOMORPH.2006.12.022.

CRED, 2018. Economic Losses, Poverty & Disasters 1998–2017.

Cui, Y., Xu, C., Xu, S., Chai, S., Fu, G., Bao, P., 2020. Small-scale catastrophic landslides in loess areas of China: an example of the March 15, 2019, Zaoling landslide in Shanxi Province. Landslides 17, 669–676. https://doi.org/10.1007/s10346-019-01322-4.

Dai, K., Xu, Q., Li, Z., Tomás, R., Fan, X., Dong, X., Li, W., Zhou, Z., Gou, J., Ran, P., 2019. Post-disaster assessment of 2017 catastrophic Xinmo landslide (China) by spaceborne SAR interferometry. Landslides 16, 1189–1199. https://doi.org/10.1007/s10346-019-01152-4.

De Vroey, M., de Vendictis, L., Zavagli, M., Bontemps, S., Heymans, D., Radoux, J., Koetz, B., Defourny, P., 2022. Mowing detection using Sentinel-1 and Sentinel-2 time series for large scale grassland monitoring. Remote Sens. Environ. 280, 113145 https://doi.org/10.1016/j.rse.2022.113145.

Deijns, A.A.J., Bevington, A.R., van Zadelhoff, F., de Jong, S.M., Geertsema, M., McDougall, S., 2020. Semi-automated detection of landslide timing using harmonic modelling of satellite imagery, Buckinghorse River, Canada. Int. J. Appl. Earth Obs. Geoinf. 84, 101943 https://doi.org/10.1016/j.jag.2019.101943.

Deijns, A.A.J., Dewitte, O., Thiery, W., D'Oreye, N., Malet, J.-P., Kervyn, F., 2022. Timing landslide and flash flood events from SAR satellite: a regionally applicable methodology illustrated in African cloud-covered tropical environments. Nat. Hazards Earth Syst. Sci. 22, 3679–3700. https://doi.org/10.5194/nhess-22-3679-2022.

Dille, A., Kervyn, F., Handwerger, A.L., D'Oreye, N., Derauw, D., Mugaruka Bibentyo, T., Samsonov, S., Malet, J.P., Kervyn, M., Dewitte, O., 2021. When image correlation is needed: Unravelling the complex dynamics of a slow-moving landslide in the tropics with dense radar and optical time series. Remote Sens. Environ. 258, 112402 https://doi.org/10.1016/j.rse.2021.112402.

Fan, X., Xu, Q., Liu, J., Subramanian, S.S., He, C., Zhu, X., Zhou, L., 2019. Successful early warning and emergency response of a disastrous rockslide in Guizhou province, China. Landslides 16, 2445–2457. https://doi.org/10.1007/s10346-019-01269-6.

Fan, X., Dufresne, A., Whiteley, J., Yunus, A.P., Subramanian, S.S., Okeke, C.A.U., Pánek, T., Hermanns, R.L., Ming, P., Strom, A., Havenith, H.B., Dunning, S., Wang, G., Tacconi Stefanelli, C., 2021. Recent technological and methodological advances for the investigation of landslide dams. Earth-Sci. Rev. 218, 103646 https://doi.org/10.1016/j.earscirev.2021.103646.

Fell, R., Corominas, J., Bonnard, C., Cascini, L., Leroi, E., Savage, W.Z., 2008. Guidelines for landslide susceptibility, hazard and risk zoning for land use planning. Eng. Geol. 102, 85–98. https://doi.org/10.1016/j.enggeo.2008.03.022.

Frantz, D., Haß, E., Uhl, A., Stoffels, J., Hill, J., 2018. Improvement of the Fmask algorithm for Sentinel-2 images: Separating clouds from bright surfaces based on parallax effects. Remote Sens. Environ. 215, 471–481. https://doi.org/10.1016/j.rse.2018.04.046.

Froude, M.J., Petley, D.N., 2018. Global fatal landslide occurrence from 2004 to 2016. Nat. Hazards Earth Syst. Sci. 18, 2161–2181. https://doi.org/10.5194/nhess-18-2161-2018.

Fu, S., de Jong, S.M., Deijns, A., Geertsema, M., de Haas, T., 2023. The SWADE model for landslide dating in time series of optical satellite imagery. Landslides 20, 913–932. https://doi.org/10.1007/s10346-022-02012-4.

Geertsema, M., Highland, L., Vaugeouis, L., 2009. Environmental impact of landslides. Landslides - Disaster Risk Reduct. 589–607. https://doi.org/10.1007/978-3-540-69970-5_31.

Guo, Z., Chen, L., Yin, K., Shrestha, D.P., Zhang, L., 2020. Quantitative risk assessment of slow-moving landslides from the viewpoint of decision-making: a case study of the three Gorges Reservoir in China. Eng. Geol. 273, 105667 https://doi.org/10.1016/j.enggeo.2020.105667.

Guzzetti, F., Reichenbach, P., Cardinali, M., Galli, M., Ardizzone, F., 2005. Probabilistic landslide hazard assessment at the basin scale. Geomorphology 72, 272–299. https://doi.org/10.1016/j.geomorph.2005.06.002.

Guzzetti, F., Peruccacci, S., Rossi, M., Stark, C.P., 2008. The rainfall intensity-duration control of shallow landslides and debris flows: An update. Landslides 5, 3–17. https://doi.org/10.1007/s10346-007-0112-1.

Guzzetti, F., Mondini, A.C., Cardinali, M., Fiorucci, F., Santangelo, M., Chang, K.T., 2012. Landslide inventory maps: new tools for an old problem. Earth-Sci. Rev. 112, 42–66. https://doi.org/10.1016/j.earscirev.2012.02.001.

Henderson, F.M., Lewis, A.J., 1998. Principles and applications of imaging radar. In: Manual of Remote Sensing, 3rd edition. John Wiley and Sons, New York.

Lu, P., Shi, W., Wang, Q., Li, Z., Qin, Y., Fan, X., 2021. Co-seismic landslide mapping using Sentinel-2 10-m fused NIR narrow, red-edge, and SWIR bands. Landslides 18, 2017–2037. https://doi.org/10.1007/s10346-021-01636-2.

McGovern, S., Brook, M.S., Cave, M., 2021. Geomorphology and triggering mechanism of a river-damming block slide: February 2018 Mangapoike landslide, New Zealand. Landslides 18, 1087–1095. https://doi.org/10.1007/s10346-020-01572-7.

Meng, Q., Intrieri, E., Raspini, F., Peng, Y., Liu, H., Casagli, N., 2022. Satellite-based interferometric monitoring of deformation characteristics and their relationship with internal hydrothermal structures of an earthflow in Zhimei, Yushu, Qinghai-Tibet Plateau. Remote Sens. Environ. 273, 112987 https://doi.org/10.1016/j.rse.2022.112987.

Mondini, A.C., Guzzetti, F., Chang, K.T., Monserrat, O., Martha, T.R., Manconi, A., 2021. Landslide failures detection and mapping using Synthetic Aperture Radar: past, present and future. Earth-Sci. Rev. 216, 103574 https://doi.org/10.1016/j.earscirev.2021.103574.

Mullissa, A., Vollrath, A., Odongo-Braun, C., Slagter, B., Balling, J., Gou, Y., Gorelick, N., Reiche, J., 2021. Sentinel-1 SAR backscatter analysis ready data preparation in Google Earth Engine. Remote Sens. 13, 1954. https://doi.org/10.3390/rs13101954.

Ostermann, M., Sanders, D., Ivy-Ochs, S., Alfimov, V., Rockenschaub, M., Römer, A., 2012. Early Holocene (8.6 ka) rock avalanche deposits, Obernberg valley (Eastern Alps): Landform interpretation and kinematics of rapid mass movement. Geomorphology 171–172, 83–93. https://doi.org/10.1016/J.GEOMORPH.2012.05.006.

Ouyang, C., Zhao, W., An, H., Zhou, S., Wang, D., Xu, Q., Li, W., Peng, D., 2019. Early identification and dynamic processes of ridge-top rockslides: implications from the Su Village landslide in Suichang County, Zhejiang Province, China. Landslides 16, 799–813. https://doi.org/10.1007/s10346-018-01128-w.

Pánek, T., 2015. Recent progress in landslide dating: a global overview. Prog. Phys. Geogr. 39, 168–198. https://doi.org/10.1177/0309133314550671.

Qu, F., Qiu, H., Sun, H., Tang, M., 2021. Post-failure landslide change detection and analysis using optical satellite Sentinel-2 images. Landslides 18, 447–455. https://doi.org/10.1007/s10346-020-01498-0.

Reiche, J., de Bruin, S., Hoekman, D., Verbesselt, J., Herold, M., 2015. A Bayesian approach to combine landsat and ALOS PALSAR time series for near real-time deforestation detection. Remote Sens. 7, 4973–4996. https://doi.org/10.3390/rs70504973.

Reiche, J., Hamunyela, E., Verbesselt, J., Hoekman, D., Herold, M., 2018a. Improving near-real time deforestation monitoring in tropical dry forests by combining dense Sentinel-1 time series with Landsat and ALOS-2 PALSAR-2. Remote Sens. Environ. 204, 147–161. https://doi.org/10.1016/j.rse.2017.10.034.

Reiche, J., Verhoeven, R., Verbesselt, J., Hamunyela, E., Wielaard, N., Herold, M., 2018b. Characterizing tropical forest cover loss using dense Sentinel-1 data and active fire alerts. Remote Sens. 10, 777. https://doi.org/10.3390/rs10050777.

Samsonov, S., Dille, A., Dewitte, O., Kervyn, F., d'Oreye, N., 2020. Satellite interferometry for mapping surface deformation time series in one, two and three dimensions: a new method illustrated on a slow-moving landslide. Eng. Geol. 266, 105471 https://doi.org/10.1016/j.enggeo.2019.105471.

Schlögel, R., Malet, J.P., Reichenbach, P., Remaître, A., Doubre, C., 2015. Analysis of a landslide multi-date inventory in a complex mountain landscape: the Ubaye valley case study. Nat. Hazards Earth Syst. Sci. 15, 2369–2389. https://doi.org/10.5194/nhess-15-2369-2015.

Šilhán, K., 2020. Dendrogeomorphology of landslides: principles, results and perspectives. Landslides 17, 2421–2441. https://doi.org/10.1007/s10346-020-01397-4.

Squarzoni, C., Delacourt, C., Allemand, P., 2003. Nine years of spatial and temporal evolution of the La Valette landslide observed by SAR interferometry. Eng. Geol. 68, 53–66. https://doi.org/10.1016/S0013-7952(02)00198-9.

Tang, C., Zhu, J., Qi, X., Ding, J., 2011. Landslides induced by the Wenchuan earthquake and the subsequent strong rainfall event: a case study in the Beichuan area of China. Eng. Geol. 122, 22–33. https://doi.org/10.1016/j.enggeo.2011.03.013.

Tucker, C.J., 1979. Red and photographic infrared linear combinations for monitoring vegetation. Remote Sens. Environ. 8, 127–150. https://doi.org/10.1016/0034-4257(79)90013-0.

Varnes and the IAEG Commission on Landslides and other Mass-Movements, 1984 D.J. Varnes, IAEG Commission on Landslides and other Mass-MovementsLandslide Hazard Zonation: a Review of Principles and PracticeNESCO Press, Paris (1984) 63 pp.

van Westen, C.J., Castellanos, E., Kuriakose, S.L., 2008. Spatial data for landslide susceptibility, hazard, and vulnerability assessment: An overview. Eng. Geol. 102, 112–131. https://doi.org/10.1016/j.enggeo.2008.03.010.

Wang, X., Fan, X., Xu, Q., Du, P., 2022. Change detection-based co-seismic landslide mapping through extended morphological profiles and ensemble strategy. ISPRS J. Photogramm. Remote Sens. 187, 225–239. https://doi.org/10.1016/j.isprsjprs.2022.03.011.

Wu, S.-T., 1984. Analysis of synthetic aperture radar data acquired over a variety of land cover. IEEE Trans. Geosci. Remote Sens. GE-22, 550–557. https://doi.org/10.1109/TGRS.1984.6499169.

Xiong, Z., Feng, G., Feng, Z., Miao, L., Wang, Y., Yang, D., Luo, S., 2020. Pre- and post-failure spatial-temporal deformation pattern of the Baige landslide retrieved from multiple radar and optical satellite images. Eng. Geol. 279, 105880 https://doi.org/10.1016/j.enggeo.2020.105880.

Xu, Q., Zhao, B., Dai, K., Dong, X., Li, W., Zhu, X., Yang, Y., Xiao, X., Wang, X., Huang, J., Lu, H., Deng, B., Ge, D., 2023. Remote sensing for landslide investigations: a progress report from China. Eng. Geol. 321, 107156 https://doi.org/10.1016/j.enggeo.2023.107156.

Yang, W., Wang, Yunqi, Sun, S., Wang, Yujie, Ma, C., 2019. Using Sentinel-2 time series to detect slope movement before the Jinsha River landslide. Landslides 16, 1313–1324. https://doi.org/10.1007/s10346-019-01178-8.

Zhao, F., Gong, W., Tang, H., Pudasaini, S.P., Ren, T., Cheng, Z., 2023. An integrated approach for risk assessment of land subsidence in Xi'an, China using optical and radar satellite images. Eng. Geol. 314, 106983 https://doi.org/10.1016/j.enggeo.2022.106983.

Zhu, Z., 2017. Change detection using landsat time series: a review of frequencies, preprocessing, algorithms, and applications. ISPRS J. Photogramm. Remote Sens. 130, 370–384. https://doi.org/10.1016/j.isprsjprs.2017.06.013.

Zhu, Z., Wang, S., Woodcock, C.E., 2015. Improvement and expansion of the Fmask algorithm: Cloud, cloud shadow, and snow detection for Landsats 4-7, 8, and Sentinel 2 images. Remote Sens. Environ. 159, 269–277. https://doi.org/10.1016/j.rse.2014.12.014.

Zhu, Y., Qiu, H., Yang, D., Liu, Z., Ma, S., Pei, Y., He, J., Du, C., Sun, H., 2021. Pre- and post-failure spatiotemporal evolution of loess landslides: a case study of the Jiangou landslide in Ledu, China. Landslides 18, 3475–3484. https://doi.org/10.1007/s10346-021-01714-5.